Electrochimica Acta 499 (2024) 144705

Contents lists available at ScienceDirect

Electrochimica Acta

journal homepage: www.journals.elsevier.com/electrochimica-acta

Evaluating the impact of iron impurities in KOH on OER performance of $BaNiO_3$ single crystals using scanning electrochemical cell microscopy

Daniel Gutiérrez-Martín [a,*], Abdelilah Asserghine [b], Almudena Torres-Pardo [a], Áurea Varela [a], Joaquín Rodríguez-López [b,*], José María González-Calbet [a], Marina Parras [a]

[a] Departamento de Química Inorgánica, Facultad de Ciencias Químicas, Universidad Complutense, 28040 Madrid, Spain
[b] Department of Chemistry, University of Illinois Urbana-Champaign, 600 S Mathews Ave., Urbana, IL 61801, USA

ARTICLE INFO

Keywords:
Scanning electrochemical cell microscopy
Oxygen evolution reaction
$BaNiO_3$
Iron impurities in KOH

ABSTRACT

Understanding the oxygen evolution reaction (OER) electrocatalysis requires a careful understanding of the surface and activity evolution of well-defined materials. An especially promising candidate is the $BaNiO_3$ hexagonal perovskite, matching strides with benchmark catalysts such as $Ba_{0.5}Sr_{0.5}Co_{0.8}Fe_{0.2}O_{3-\delta}$. Here, we conducted a structural and electrochemical analysis of $BaNiO_3$ single crystals to assess the influence of iron impurities in KOH electrolyte on their OER performance. We used scanning electrochemical cell microscopy (SECCM) for precise measurements on $BaNiO_3$ single crystals in the absence of carbon additives. Cyclic voltammetry (CV) revealed that the presence of iron consistently enhanced the OER current with subsequent cycles, indicating a dynamic improvement in $BaNiO_3$'s electrochemical activity. Conversely, in iron-free KOH electrolyte, performance diminished with cycling. These findings not only underscore the critical necessity of KOH purification for $BaNiO_3$ electrochemical studies but also showcase SECCM's unparalleled ability to offer insights into the electrochemical evolution of individual entities such as single crystals. This makes it a powerful *operando* tool for evaluating forthcoming single crystals, thereby aiding in the design of superior catalysts for OER reactions.

1. Introduction

Exploiting safe, clean, and sustainable energy sources is a major societal and technological challenge in the 21st century. In this context, hydrogen emerged as a green alternative to fossil fuels [1–3]. Major hydrogen-generation technologies include natural gas reforming, coal gasification and water electrolysis [4]. To replace fossil fuels, water electrolysis is particularly important since it produces high-purity hydrogen (>99 %) while keeping the CO_2 emissions at minimal levels. More importantly, it can be easily coupled with current environmentally responsible energies such as wind, solar and hydroelectric, transforming surplus energy into hydrogen [5]. Nevertheless, one of the bottlenecks of electrochemical water splitting technologies is the oxygen evolution reaction (OER). In basic media, the OER involves a four-electron transfer ($4OH^- \rightarrow O_2 + 2H_2O + 4e^-$), which often displays slow kinetics. Current benchmark catalysts often incorporate noble metals such as ruthenium or iridium, underscoring the necessity for the development of new cost-effective materials [6,7]. Furthermore, exploring the intrinsic catalytic properties is essential for understanding their true activity, laying the groundwork for subsequent optimization through factors like morphology and composition design [8–11]. Single crystal systems are particularly useful as they present a performance reference to be compared with modern tailored catalysts. Additionally, they tend to simplify the involved processes in comparison to nanoparticulated systems, enabling the establishment of new structure-activity relationships [12].

On this matter, $BaNiO_3$ has been brought up to the scientific spotlight recently owing to its OER capabilities. Initially, a $BaNiO_3$ single crystal was prepared by J.G. Lee *et al.* [13] using a well-known flux method described by J. Lander [14]. This phase seems especially active, and its surface normalized OER performance surpasses perovskite benchmark material $Ba_{0.5}Sr_{0.5}Co_{0.8}Fe_{0.2}O_{3-\delta}$ [15]. Moreover, its synthesis does not depend on critical raw elements such as cobalt or lanthanides, fulfilling the European Union requirements [16]. Nevertheless, it is generally known that the presence of iron impurities strongly affects electrocatalytic measurements of nickel and cobalt materials [17–19]. This

* Corresponding authors.
E-mail addresses: dangut04@ucm.es (D. Gutiérrez-Martín), joaquinr@illinois.edu (J. Rodríguez-López).

https://doi.org/10.1016/j.electacta.2024.144705
Received 28 May 2024; Received in revised form 9 July 2024; Accepted 10 July 2024
Available online 14 July 2024

aspect has been thoroughly studied in hydroxides, exhibiting activities orders of magnitude higher when in the presence of impurities coming from the KOH electrolyte. However, in none of the Ba-Ni-O electrocatalysis works [13,20–22] iron purified electrolyte has been explicitly used to carry out the electrocatalytic experiments, begging the question of whether iron impurities strongly affect the $BaNiO_3$ single crystals.

The electrochemical performance of single crystals catalysts is commonly measured using a rotating disk electrode (RDE) [23–25]. The RDE allows for quick and simple measurements with minimal equipment requirements. Despite these advantages, the RDE also presents major drawbacks, one of them being the need for ink preparation for catalyst evaluation [26]. This ink formulation commonly contains carbon black as a conductive support and Nafion as a binder, whose concentrations are not standardized. It has been demonstrated that they enhance the catalyst stability and performance and that they do participate in ORR [27,28] while their influence on OER remains unclear yet [29]. As a result, the systematical development of electrocatalysts ultimately demands performance evaluation without additives, which is not possible for conventional RDE measurements due to the catalysts' lack of adhesion to the glassy carbon.

A viable approach is presented in scanning electrochemical cell microscopy (SECCM) [30]. While in classical RDE measurements, the catalyst particles are completely submerged in the electrolyte, SECCM removes the need for a macroscopic cell altogether. In the simplest version of this technique, a micropipette with a small orifice at the end is filled with the desired electrolyte solution and is made contact against the sample. Forming a meniscus of contact size similar to that of the orifice. That contact is made to act as the working electrode, while a counter/reference electrode is placed within the micropipette to complete the circuit and perform electrochemical experiments [31]. In this way, individual entities, such as single crystals deposited on a conductive substrate as is done here, can be directly addressed electrochemically, eliminating the need for binders. Control over the micropipette orifice size using a variety of heated pulling methods allows this technique to be tailored to the particle size of the material for single-particle measurements, maximizing compatibility [31–33].

In this work, we use SECCM measurements to study the influence of iron impurities in KOH electrolyte on the OER performance of $BaNiO_3$ single crystals. In addition, we determine by electron microscopy techniques the presence of a nickel-rich surface that can explain previous research concerning this oxide structure [34].

2. Experimental

2.1. Synthesis procedure

Several publications describe the synthesis of $BaNiO_3$ single crystals using the KOH flux method. As described by Choi *et al.* [35], the reagents ratio and cooling slope can be tuned to control the morphology of the obtained crystals. According to the described synthesis conditions, the optimal $BaNiO_3$ precursor-to-KOH ratio to obtain hexagonal prism single crystals of $BaNiO_3$ is 1:50. Nonetheless, we followed a similar procedure to L. Jin et al. [34], to reproduce the hydroxide-containing oxide. 3,96 g of barium carbonate (20 mmol, Sigma Aldrich, 99,98 %) and 1,5 g of nickel oxide (20 mmol, Sigma Aldrich, 99,99) were ground together and thermally treated overnight at 1000 °C and then at 1100 °C for 24 h in a muffle furnace. 0,5 g of the obtained greenish precursor and 0,5 g of $Ba(OH)_2{\cdot}8H_2O$ were mixed with 50 g of KOH (0,89 mol, Sigma Aldrich, 99,99 %) and thermally treated for 24 h at 700 °C in an Al_2O_3 crucible with a heating slope of 3 °C/min. Then, the oven is cooled down to room temperature at 0,3 °C/min. The obtained solid was washed several times with deionized water and vacuum-filtered to obtain golden-green needle-shaped crystals.

2.2. X-ray single crystal diffraction

A needle-like specimen of $BaNiO_3$ (0.009×0.018×0.237 mm) was used for the X-Ray crystallographic analysis. Single crystal X-ray diffraction (XRD) data collection was carried out at room temperature on a Bruker D8 Venture diffractometer in the UCM CAI for XRD facilities, using Cu Kα radiation (λ = 1.54184 Å) from an ImuS3.0 Incoatec microfocus sealed tube operating at 50 kV. A total of 3747 reflections were collected during a total exposure time of 5.83 h.

2.3. Powder X-ray diffraction

The obtained crystals were grounded until a fine powder was obtained to collect powder X-ray diffraction data. The diffractometer used was a Bruker D8 Advance A25 model working with a Copper tube in line focus, an incident focusing mirror and a "LynxEye SSD160–2″ fast detector located at the X-ray diffraction facilities of the Universidad Complutense de Madrid (Spain). The phase identification analysis of the collected diffractograms was done with the help of the X'Pert HighScore software [36] in combination with the ICDD PDF5+ database (International Center for Diffraction Data, release 2024) [37].

2.4. Scanning electron microscopy, scanning electron transmission microscopy and energy dispersive X-ray spectroscopy

Electron microscopy was performed using a variety of equipment situated in the National Facility ELECMI ICTS facilities. The morphological study and cationic composition were studied by scanning electron microscopy (SEM) and energy dispersive X-ray spectroscopy (EDS) using JEOL JSM 7600F and JEOL JSM IT700HR microscopes equipped with 170 mm^2 Oxford Ultratim and Oxford DrySD™ 60mm^2 detectors respectively operating at an acceleration voltage of 15 kV. Selected area electron diffraction (SAED) and high resolution transmission electron microscopy (HRTEM) were performed using JEOL 2100 HT and JEOL JEM 3000F electron microscopes. Scanning transmission electron microscopy (STEM) and STEM-EDS chemical microanalysis were carried out on a JEOL JEM 3000F electron microscope supplied with an Oxford Xplore TEM detector.

2.5. X-ray photoelectron spectroscopy

X-ray photoelectron spectroscopy (XPS) analysis was carried out in a SPECS spectrometer with an MCD-9 detector, using a non-monochromatic Mg K_α source. The XPS data was treated using the CasaXPS software[38] and the binding energy values were referenced to adventitious carbon.

2.6. Scanning electrochemical cell microscopy

All SECCM measurements were conducted using the CHI-920D scanning electrochemical microscope. The SECCM probe consisted of a micropipette with an opening diameter of 80 μm. These micropipettes were fabricated by pulling borosilicate glass capillaries using the Sutter Instruments Puller Model P-2000. The parameters used for pulling the capillaries were as follows: heat = 300, filament = 4, velocity = 20, delay = 140, pull = 0. To facilitate the identification of individual $BaNiO_3$ single crystals, which vary in size from 5 μm to 200 μm in length, a camera was employed. All SECCM measurements were performed using a personal computer (PC).

A 0.1 M KOH (VWR Chemicals, 88 %, <0.001 % Fe, Lot: 23B0856207) solution is used as non-purified electrolyte. Purification of the electrolyte to avoid iron impurities was carried out by nickel hydroxide synthesized from $Ni(NO_3)_2{\cdot}6H_2O$ (Sigma Aldrich, 99,999 %) following Trotochaud's protocol [17].

Voltammograms are represented according to the polarographic convention, in which anodic currents present negative values and

anodic potentials exhibit positive values.

3. Results and discussion

3.1. Structural and chemical characterization

We confirmed the structure of our $BaNiO_3$ samples by collecting single crystal X-Ray diffraction data from golden-brown needle-like crystals (**Figure S1(a)** and **(b)**) with Ba:Ni ratio close to 1:1 determined by SEM-EDS. The obtained cell parameters ($a = 5.6415$ Å, $c = 4.7917$ Å) and hexagonal symmetry (S.G. $P6_3/mmc$) are consistent with the ones previously described by Takeda *et al.* ($a = 5.632$ Å, $c = 4.809$ Å) [39]. A second and less abundant type of crystals was observed under the microscope in the form of cubes (Figure **S1(b)**). Diffraction data of these crystals ($a = 4205$ Å; S.G. *Fm*-3 *m*) can be assigned to NiO (COD: 4,320, 508), revealing the presence of this impurity in the sample. To confirm the presence of crystalline impurities, the sample is ground to collect powder X-ray diffraction data. As presented in **Figure S2**, three crystalline phases can be identified, orthorhombic $BaCO_3$ (S.G. *Pbnm*), as well as previously characterized $BaNiO_3$ and NiO.

The crystals' morphologies and compositions were further evaluated by SEM and EDS. Three types of particles are observed, elongated hexagonal prisms containing both metallic cations (Fig. 1(a)), micrometer-sized cube-shaped particles containing only nickel (**Figure S2(a)**), and elongated particles containing only barium (**Figure S2(b)**). These three morphologies can be qualitatively assigned through their composition determined by EDS to $BaNiO_3$ and known impurities NiO and $BaCO_3$ respectively (**Figure S2 (c)** and **(d)**). The obtained hexagonal prism faceted morphology for $BaNiO_3$ is consistent with the literature [35]. A closer look at the $BaNiO_3$ crystal's surface (Fig. 1(b)) reveals a rough hair-like morphology that surrounds most of its surface. Crystal-to-crystal EDS analysis was performed to confirm the expected cationic ratio (Ba:Ni = 1:1) according to its chemical formula. Unexpectedly, an average of 7 % nickel excess is observed in every hexagonal crystal containing barium and nickel.

To study this discrepancy, transmission electron microscopy (TEM) was performed in ground $BaNiO_3$ single crystal specimens. The crystals grew along the <001> direction, as shown in the electron diffraction pattern and HRTEM image depicted in Fig. 1(c) and **(d)**, in which the 2H stacking sequence is shown. $BaNiO_3$ structure is further confirmed by the presence of the [001] projection (Fig. 1(e) and **(f)**), consistent with the expected structural features. STEM-EDS was performed in multiple crystals to assess the surface composition. Once again, the crystal showed a higher nickel-to-barium ratio than expected according to the nominal composition. Point analyses across the crystal (Fig. 2(a)) confirmed a significant increase in nickel content on the crystal's surface, as shown in the STEM-EDS data (Fig. 2(c)). This feature is further confirmed by STEM-EDS chemical maps (**Figure S4(a)** and **(b)**), in which $BaNiO_3$ is shown to present a nickel-rich surface. Similar microstructural characteristics have been recently found in $BaNiO_3$ nanoparticles [40].

XPS was performed to assess the composition of the nickel surface of the $BaNiO_3$ crystals (**Figure S5**). The Ni 2p region suggests the presence of 3 different nickel species: Ni^{4+} $2p_{3/2}$ (855.5 eV) coming from $BaNiO_3$ [41], Ni^{2+} $2p_{3/2}$ (854.8 eV) from $Ni(OH)_2$ [42] and Ni^{2+} $2p_{3/2}$ (852.6 eV) from NiO [43]. The presence of a hydroxide is further confirmed by the shift to higher binding energy by the presence of an O 1 s OH signal at 531.1 eV. This hydroxide is not observed as an isolated particle; thus, it must come from the amorphous Ni^{2+} layer covering the $BaNiO_3$ crystals. A complete analysis of Ba 3d, Ni 2p and O 1 s regions is presented in the supplementary information. It has been proposed that a hydroxide within the $BaNiO_3$ crystalline structure may be present [34]. In this regard, the structural characterization performed in this work points out the presence of an amorphous nickel hydroxide layer that may be formed during the cooling process of the synthesis, and that could explain previously published data [34].

3.2. Electrochemical characterization

To explore the effects of iron impurities on $BaNiO_3$ single crystals, we utilized the SECCM technique. In our experimental setup, $BaNiO_3$ single crystals were deposited onto an indium-tin oxide (ITO) substrate. An SECCM probe, comprised of a solution-filled micropipette, selectively made contact with individual single crystals on the substrate, as depicted in Fig. 3.

The SECCM measurement employed a micropipette with an opening

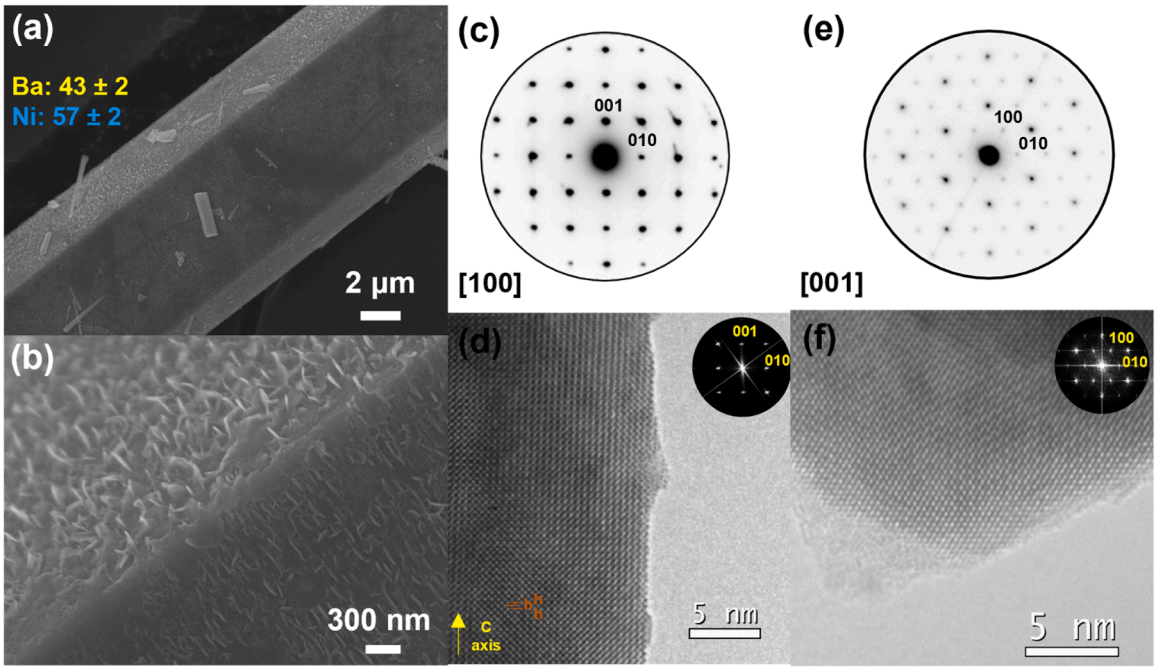

Fig. 1. SEM micrographs **(a)** and **(b)** and cationic ratio obtained by EDS. SAED **(c)** and HRTEM image **(d)** of the [100] projection. SAED **(e)** and HRTEM image **(f)** of the [001] projection. 2H packing sequence along the c axis is signaled in **(d)** in brown.

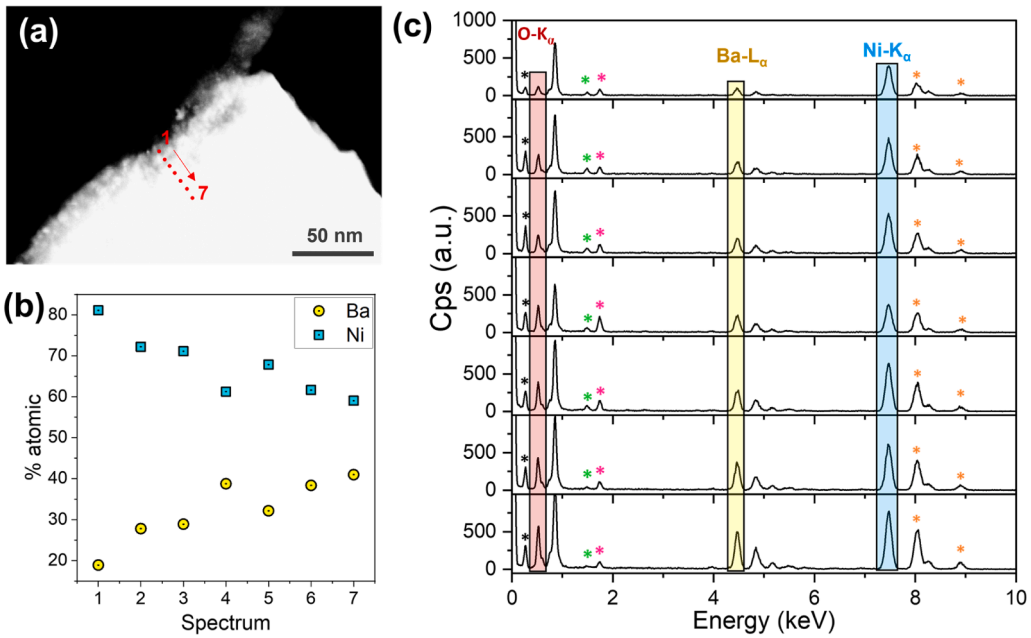

Fig. 2. Annular dark field image **(a)** of a $BaNiO_3$ crystal's surface. STEM-EDS point **(b)** results obtained from Ba-L_α and Ni-K_α. The areas in which point EDS analysis is performed are marked with red dots. The EDS spectrum of each point from the punctual analysis is presented in **(c).** Additional signals of **(c)** are marked as asterisks: C-K_α (black), Al-K_α (green), Si-K_α (pink), and Cu-K_α and Cu-K_β (orange) signals.

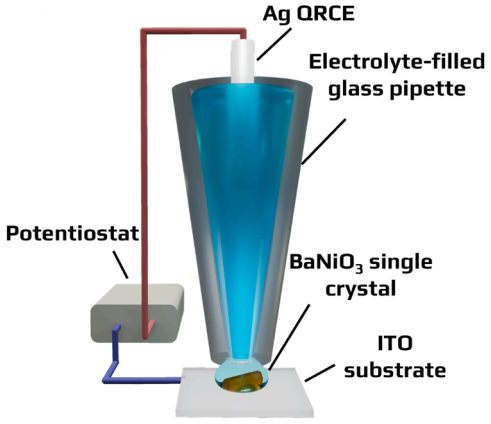

Fig. 3. Scheme depicting the SECCM setup. Purified and non-purified 0.1 M KOH used as electrolyte.

diameter of 80 μm, filled with either purified or unpurified KOH solution. This micropipette was connected to an Ag wire, acting as the quasi-reference counter electrode (QRCE), as illustrated in Fig. 3. A camera was utilized to identify and select individual crystals, according to their color, morphology and size, allowing for impurity discrimination (such as NiO cubic crystals) among the obtained crystals (**Figure S6**). Upon contact with the $BaNiO_3$ single crystal, a meniscus formed between the micropipette and the ITO substrate. This meniscus facilitated the electrochemical measurements of the $BaNiO_3$ single crystals in a two-electrode configuration, with the ITO/$BaNiO_3$ serving as the working electrode (WE) and Ag as the QRCE.

Initially, we conducted 10 successive cyclic voltammograms (CVs) ranging from 0 to 1 V vs QRCE on an ITO substrate using a micropipette filled with non-purified KOH, as shown in **Figure S7**. These CVs exhibited only a small increase in current at higher potentials (0.8–1 V vs QRCE) owing to the OER. However, when the 20 CV cycles in the same range were conducted on $BaNiO_3$ single crystals with non-purified KOH, a distinct redox wave emerged in the 0.3–0.6 V vs QRCE region. This redox wave was attributed to the oxidation and reduction processes involving surface Ni^{2+} [17]. Additionally, a significantly larger anodic current emerged around 0.7 V vs QRCE, corresponding to the OER [13]. This OER current is expected, as $BaNiO_3$ is an active catalyst towards this reaction. Remarkably, as cycling progressed, both the Ni^{2+} and OER peaks exhibited a notable increase in intensity, as depicted in the accompanying Fig. 4(a). This observation suggests a dynamic enhancement in the electrochemical activity of the $BaNiO_3$ single crystals over successive cycles. A similar trend was observed by J. G. Lee *et al.* and assessed to nickel oxide exsolution by reduction of $BaNiO_3$ to $Ba_6Ni_5O_{15}$ [13].

In contrast, the CV experiments conducted with purified KOH on $BaNiO_3$ single crystals, shown in Fig. 4(b), demonstrated a different behavior. Despite observing similar redox peaks, there was minimal variation in the peak intensities within the first cycles, followed by a decrease in current as the experiment progressed. A comparison between normalized current values of the first CV cycle at a fixed potential ($E = 1$ V vs Ag QRCE) is presented in Fig. 4(c), highlighting the differences in electrochemical response between the purified and non-purified KOH solutions. To confirm this assessment, each measurement was replicated three times in non-purified and iron-purified KOH electrolytes as depicted in **Figures S8** and **S9** respectively, showing each time the same behavior and differences. It is worth noting that the difference in current magnitude between purified and unpurified KOH during the initial cycles may not be attributable to activity but rather to the size of individual crystals. However, the observed trends in purified and non-purified KOH remain consistent regardless of crystal size. The differing trend observed in purified and unpurified KOH in response cannot be attributed to nickel oxide exsolution, as it would not discriminate between electrolytes and would occur in both.

This disparity in the response between unpurified and purified KOH emphasizes the influential role of iron impurities on the electrochemical performance of $BaNiO_3$ single crystals. A plausible explanation of this distinction has been established for other heavily studied nickel materials. In $LaNiO_3$, a significant surface modulation of the catalyst occurs when OER is performed in the presence of trace iron [44,45]. This surface evolution is caused by the leaching of lanthanum, which generates an amorphous NiOOH superficial layer in which iron incorporates. This phenomenon has also been demonstrated in plain NiOOH, which can

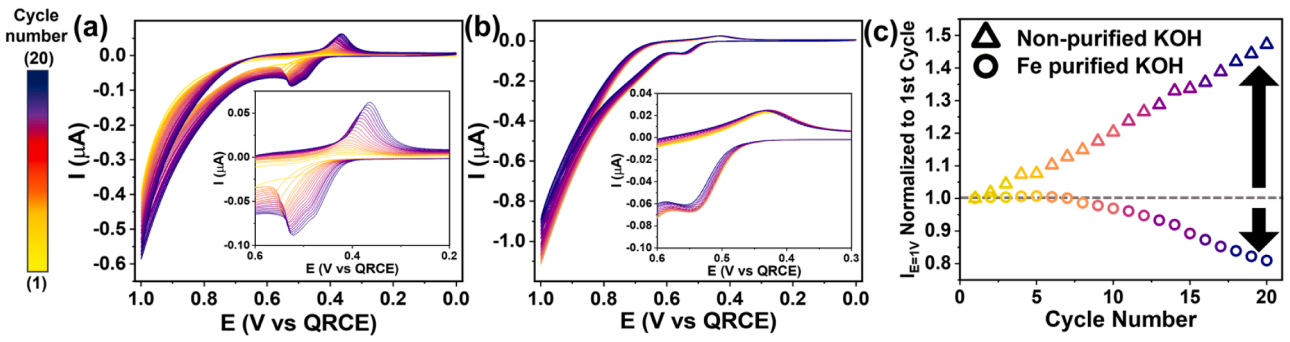

Fig. 4. SECCM CV performed in non-purified KOH electrolyte **(a)** and iron-purified electrolyte **(b)**. Inset graphs are included from the Ni^{2+}/Ni^{3+} region. Normalized current values at $E = 1$ V vs QSRE versus the first cycle current (−0.39 and −1.10 μA respectively) comparison between non-purified and iron-purified KOH electrolyte **(c)**. Experimental conditions: $\nu = 50$ mV/s; [KOH]:0.1 M; micropipette size: 80 μm.

dynamically adsorb iron even after only one CV cycle after spiking iron into a KOH iron-free electrolyte [46]. This absorption ultimately can result in surface reconstruction, leading to the formation of a mixed iron-nickel oxyhydroxide [47]. $BaNiO_3$ single crystals grown by the flux method would be able to undergo both pathways. On the one hand, barium as well as other alkaline earths are less stable than lanthanum in OER conditions, making them more prone to leaching (Fig. 5(a)) [48, 49]. Additionally, as proven by the structural characterization performed on the samples, a $Ni(OH)_2$ surface layer is present in the flux-grown crystals, allowing for instantaneous iron incorporation (Fig. 5(b)).

Post-catalysis structural characterization by TEM was attempted on the measured $BaNiO_3$ single crystals. Nevertheless, several concerns are raised regarding the crystals' manipulation and identification within the TEM grid. Similar difficulties were enunciated by other authors [50] and surpassed by a particle-at-the-stick methodology, which is not viable in our case by our crystals' size.

4. Conclusions

In summary, we first performed a complete structural and chemical characterization of $BaNiO_3$ single crystals, by diffractometric, spectroscopic and electron microscopy techniques. We have demonstrated the presence of an amorphous $Ni(OH)_2$ layer on the crystals surface, which can influence OER performance. Then, we have performed SECCM experiments to assess the influence of iron impurities in commercial KOH in OER performance without the influence of carbon additives. These experiments clearly show an increase in activity as the $BaNiO_3$ is cycled in OER conditions when the KOH is not iron-purified. These experiments underscore the significant impact of iron impurities on the electrochemical behavior of $BaNiO_3$ single crystals, highlighting the importance of purity in the electrolyte for accurate electrochemical characterization. Importantly, it demonstrated the capacity of the SECCM technique to provide deep insights into the electrochemical characteristics of individual single crystals positions it as a potent operational tool for assessing upcoming single crystals. Consequently, it contributes significantly to the development of advanced catalyst designs for OER reactions.

CRediT authorship contribution statement

Daniel Gutiérrez-Martín: Writing – review & editing, Writing – original draft, Methodology, Investigation, Formal analysis, Conceptualization. **Abdelilah Asserghine:** Writing – review & editing, Writing – original draft, Supervision, Methodology, Formal analysis, Conceptualization. **Almudena Torres-Pardo:** Writing – review & editing, Investigation, Formal analysis. **Áurea Varela:** Writing – review & editing, Supervision. **Joaquín Rodríguez-López:** Writing – review & editing, Supervision, Funding acquisition. **José María González-Calbet:** Resources, Funding acquisition. **Marina Parras:** Writing – review & editing, Supervision.

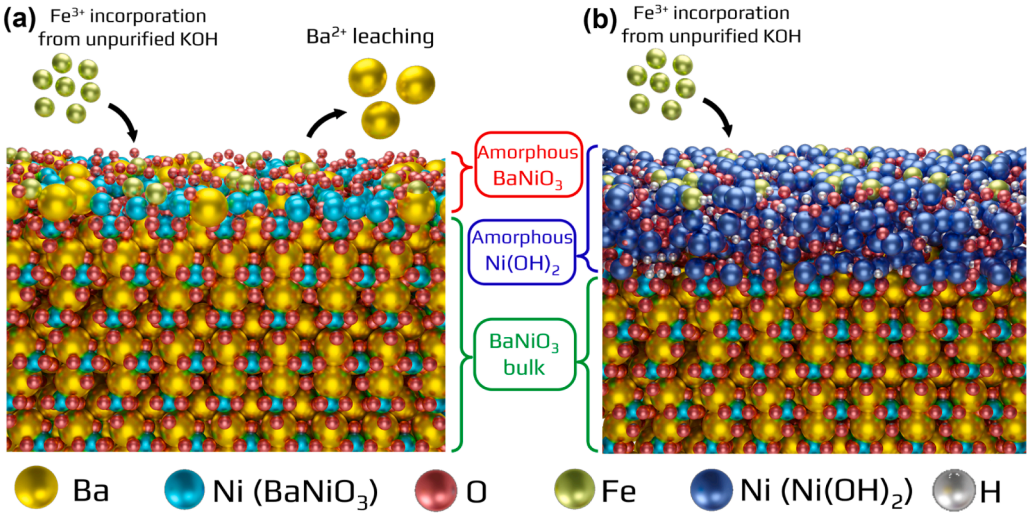

Fig. 5. Pathways of Fe^{3+} incorporation into $BaNiO_3$ **(a)** and $Ni(OH)_2$ surface-modified $BaNiO_3$ **(b).** In $BaNiO_3$ **(a)**, surface is amorphized due to barium leaching and iron is incorporated. In flux-grown $BaNiO_3$ **(b),** the surface presents an amorphous $Ni(OH)_2$ layer in which iron is incorporated.

Declaration of competing interest

The authors declare that they have no known competing financial interests or personal relationships that could have appeared to influence the work reported in this paper.

Data availability

Data will be made available on request.

Acknowledgements

The authors acknowledge the support from the "(MAD2D-CM)-UCM" project funded by Comunidad de Madrid, by the Recovery, Transformation and Resilience Plan, and by Next Generation EU from the European Union and from the Ministerio de Ciencia, Innovación y Universidades through Research Project PID2020–113753RB-I00. D.G.-M. acknowledges financial support from CT63/19-CT64/19 Complutense fellowship. We thank the National Facility ELECMI ICTS and CAI for XRD (UCM) for facilities. Patricia Delgado-Martínez is thanked for single crystal data collection. This material is based upon the work supported by the National Science Foundation under CHE Grant No. 2004054.

Supplementary materials

Supplementary material associated with this article can be found, in the online version, at doi:10.1016/j.electacta.2024.144705.

References

[1] H.D. Yoo, E. Markevich, G. Salitra, D. Sharon, D. Aurbach, On the challenge of developing advanced technologies for electrochemical energy storage and conversion, Mater. Today 17 (2014) 110–121, https://doi.org/10.1016/j.mattod.2014.02.014.
[2] H. Fayaz, R. Saidur, N. Razali, F.S. Anuar, A.R. Saleman, M.R. Islam, An overview of hydrogen as a vehicle fuel, Renew. Sustain. Ener. Rev. 16 (2012) 5511–5528, https://doi.org/10.1016/j.rser.2012.06.012.
[3] G.W. Crabtree, M.S. Dresselhaus, M.V. Buchanan, The hydrogen economy, Phys Today 57 (2004) 39–44, https://doi.org/10.1063/1.1878333.
[4] A. Ajanovic, M. Sayer, R. Haas, The economics and the environmental benignity of different colors of hydrogen, Int. J. Hydr. Ener. 47 (2022) 24136–24154, https://doi.org/10.1016/j.ijhydene.2022.02.094.
[5] S. Shiva Kumar, H. Lim, An overview of water electrolysis technologies for green hydrogen production, Ener. Rep. 8 (2022) 13793–13813, https://doi.org/10.1016/j.egyr.2022.10.127.
[6] C. Minke, M. Suermann, B. Bensmann, R. Hanke-Rauschenbach, Is iridium demand a potential bottleneck in the realization of large-scale PEM water electrolysis? Int. J. Hydro. Ener. 46 (2021) 23581–23590, https://doi.org/10.1016/j.ijhydene.2021.04.174.
[7] R. Kleijn, E. Van Der Voet, Resource constraints in a hydrogen economy based on renewable energy sources: an exploration, Renew. Sustain. Ener. Rev. 14 (2010), https://doi.org/10.1016/j.rser.2010.07.066.
[8] T. Maiyalagan, K.R. Chemelewski, A. Manthiram, Role of the morphology and surface planes on the catalytic activity of spinel limn1.5ni0.5o4 for oxygen evolution reaction, ACS. Catal. 4 (2014) 421–425, https://doi.org/10.1021/cs400981d.
[9] Y. Li, F.M. Li, X.Y. Meng, S.N. Li, J.H. Zeng, Y. Chen, Ultrathin Co3O4 nanomeshes for the oxygen evolution reaction, ACS. Catal. 8 (2018) 1913–1920, https://doi.org/10.1021/acscatal.7b03949.
[10] O. Diaz-Morales, I. Ledezma-Yanez, M.T.M. Koper, F. Calle-Vallejo, Guidelines for the rational design of ni-based double hydroxide electrocatalysts for the oxygen evolution reaction, ACS. Catal. 5 (2015) 5380–5387, https://doi.org/10.1021/acscatal.5b01638.
[11] Q. Zhou, Y. Chen, G. Zhao, Y. Lin, Z. Yu, X. Xu, X. Wang, H.K. Liu, W. Sun, S. X. Dou, Active-site-enriched iron-doped nickel/cobalt hydroxide nanosheets for enhanced oxygen evolution reaction, ACS. Catal. 8 (2018) 5382–5390, https://doi.org/10.1021/acscatal.8b01332.
[12] A.P. O'Mullane, From single crystal surfaces to single atoms: investigating active sites in electrocatalysis, Nanoscale 6 (2014) 4012–4026, https://doi.org/10.1039/c4nr00419a.
[13] J.G. Lee, J. Hwang, H.J. Hwang, O.S. Jeon, J. Jang, O. Kwon, Y. Lee, B. Han, Y. G. Shul, A New Family of Perovskite Catalysts for Oxygen-Evolution Reaction in Alkaline Media: BaNiO3 and BaNi0.83O2.5, J. Am. Chem. Soc. 138 (2016) 3541–3547, https://doi.org/10.1021/jacs.6b00036.
[14] J.J. Lander, The crystal structures of NiO. 3BaO, NiO. BaO, BaNiO3 and intermediate phases with composition near Ba2Ni2O5; with a note on NiO, Acta Acta Crystallographica 4 (1951) 148, https://doi.org/10.1107/S0365110x51000441.
[15] F. Abdelghafar, X. Xu, S.P. Jiang, Z. Shao, Perovskite for Electrocatalytic Oxygen Evolution at Elevated Temperatures, ChemSusChem. (2024), https://doi.org/10.1002/cssc.202301534.
[16] E. Commission, Study on the EU's list of critical raw materials (2020) final report, (2020). https://doi.org/10.2873/904613.
[17] L. Trotochaud, S.L. Young, J.K. Ranney, S.W. Boettcher, Nickel-Iron oxyhydroxide oxygen-evolution electrocatalysts: the role of intentional and incidental iron incorporation, J. Am. Chem. Soc. 136 (2014) 6744–6753, https://doi.org/10.1021/ja502379c.
[18] M.S. Burke, M.G. Kast, L. Trotochaud, A.M. Smith, S.W. Boettcher, Cobalt-Iron (Oxy)hydroxide oxygen evolution electrocatalysts: the role of structure and composition on activity, stability, and mechanism, J. Am. Chem. Soc. 137 (2015) 3638–3648, https://doi.org/10.1021/jacs.5b00281.
[19] S. Klaus, Y. Cai, M.W. Louie, L. Trotochaud, A.T. Bell, Effects of Fe electrolyte impurities on Ni(OH)2/NiOOH structure and oxygen evolution activity, J. Phy. Chem. C 119 (2015) 7243–7254, https://doi.org/10.1021/acs.jpcc.5b00105.
[20] J.G. Lee, H.J. Hwang, O. Kwon, O.S. Jeon, J. Jang, Y.G. Shul, Synthesis and application of hexagonal perovskite BaNiO3 with quadrivalent nickel under atmospheric and low-temperature conditions, Chem. Commun. 52 (2016) 10731–10734, https://doi.org/10.1039/c6cc05704g.
[21] M. Retuerto, F. Calle-Vallejo, L. Pascual, P. Ferrer, Á. García, J. Torrero, D. Gianolio, J.L.G. Fierro, M.A. Peña, J.A. Alonso, S. Rojas, Role of lattice oxygen content and Ni geometry in the oxygen evolution activity of the Ba-Ni-O system, J. Pow. Sourc. 404 (2018) 56–63, https://doi.org/10.1016/j.jpowsour.2018.09.098.
[22] J. Junita, D. Jayalakshmi, J.D. Rodney, Combustion-derived BaNiO3 nanoparticles as a potential bifunctional electrocatalyst for overall water splitting, Int. J. Hydro. Ener. (2023), https://doi.org/10.1016/j.ijhydene.2022.12.291.
[23] F. Opekar, P. Beran, Rotating disk electrodes, J. Electroanal. Chem. (1976) 1–105, https://doi.org/10.1016/S0022-0728(76)80129-5.
[24] K. Shinozaki, J.W. Zack, R.M. Richards, B.S. Pivovar, S.S. Kocha, Oxygen reduction reaction measurements on platinum electrocatalysts utilizing rotating disk electrode technique, J. Electrochem. Soc. 162 (2015) F1144–F1158, https://doi.org/10.1149/2.1071509jes.
[25] M.F. Tesch, S. Neugebauer, P.V. Narangoda, R. Schlögl, A.K. Mechler, The rotating disc electrode: measurement protocols and reproducibility in the evaluation of catalysts for the oxygen evolution reaction, Ener. Adv. 2 (2023) 1823–1830, https://doi.org/10.1039/d3ya00340j.
[26] K. Shinozaki, J.W. Zack, S. Pylypenko, B.S. Pivovar, S.S. Kocha, Oxygen reduction reaction measurements on platinum electrocatalysts utilizing rotating disk electrode technique, J. Electrochem. Soc. 162 (2015) F1384–F1396, https://doi.org/10.1149/2.0551512jes.
[27] D.M. Morales, J. Villalobos, M.A. Kazakova, J. Xiao, M. Risch, Nafion-induced reduction of manganese and its impact on the electrocatalytic properties of a highly active mnfeni oxide for bifunctional oxygen conversion**, (2021). https://doi.org/10.26434/chemrxiv.14696463.v1.
[28] G. Kéranguéven, C. Bouillet, V. Papaefthymiou, P.A. Simonov, E.R. Savinova, How key characteristics of carbon materials influence the ORR activity of LaMnO3- and Mn3O4-carbon composites prepared by in situ autocombustion method, Electrochim. Acta 353 (2020), https://doi.org/10.1016/j.electacta.2020.136557.
[29] N. Kakati, L. Anderson, G. Li, D.M. Sua-An, A. Karmakar, J.D. Ocon, P.Y.A. Chuang, Indispensable Nafion ionomer for high-efficiency and stable oxygen evolution reaction in alkaline media, ACS. Appl. Mater. Interf. 15 (2023) 55559–55569, https://doi.org/10.1021/acsami.3c08377.
[30] A.G. Güell, S.C.S. Lai, K. McKelvey, M.E. Snowden, P.R. Unwin, Scanning electrochemical cell microscopy: a versatile technique for nanoscale electrochemistry and functional imaging neil ebejer1, Ann. Rev. Anal. Chem. 6 (2013) 329–351, https://doi.org/10.1146/annurev-anchem-062012-092650.
[31] O.J. Wahab, M. Kang, P.R. Unwin, Scanning electrochemical cell microscopy: a natural technique for single entity electrochemistry, Curr. Opin. Electrochem. 22 (2020) 120–128, https://doi.org/10.1016/j.coelec.2020.04.018.
[32] M.V. Mirkin, T. Sun, Y. Yu, M. Zhou, Electrochemistry at one nanoparticle, Acc. Chem. Res. 49 (2016) 2328–2335, https://doi.org/10.1021/acs.accounts.6b00294.
[33] J. Kim, C. Renault, N. Nioradze, N. Arroyo-Currás, K.C. Leonard, A.J. Bard, Electrocatalytic activity of individual Pt nanoparticles studied by nanoscale scanning electrochemical microscopy, J. Am. Chem. Soc. 138 (2016) 8560–8568, https://doi.org/10.1021/jacs.6b03980.
[34] L. Jin, H. Wang, X. Xu, D. Ni, C. Yang, Y.C. Ku, C.E. Liu, C.Y. Kuo, C.F. Chang, R. Sereika, W. Bi, W. Xie, R.J. Cava, Hidden hydroxides in KOH-grown BaNiO3 crystals: a potential link to their catalytic behavior, Chem. Mater. 35 (2023) 9434–9443, https://doi.org/10.1021/acs.chemmater.3c02482.
[35] J.Y. Choi, J.H. Cho, J.W. Sun, H.P. Kim, J. Ryu, Y.E. Durmus, H. Tempel, R. A. Eichel, W. Jo, Morphology control of high-quality hexagonal perovskite BaNiO3 by molten salt method, Mater. Today Chem. 32 (2023), https://doi.org/10.1016/j.mtchem.2023.101645.
[36] T. Degen, M. Sadki, E. Bron, U. König, G. Nénert, The high score suite. Powder Diffr, Cambridge University Press, 2014, pp. S13–S18, https://doi.org/10.1017/S0885715614000840.
[37] S. Gates-Rector, T. Blanton, The Powder Diffraction File: a quality materials characterization database, Powd. Diffr. 34 (2019) 352–360, https://doi.org/10.1017/S0885715619000812.

[38] N. Fairley, V. Fernandez, M. Richard-Plouet, C. Guillot-Deudon, J. Walton, E. Smith, D. Flahaut, M. Greiner, M. Biesinger, S. Tougaard, D. Morgan, J. Baltrusaitis, Systematic and collaborative approach to problem solving using X-ray photoelectron spectroscopy, Appl. Surf. Sci. Adv. 5 (2021), https://doi.org/10.1016/j.apsadv.2021.100112.

[39] Y. Takeda, F. Kanamaru, M. Shimada, M. Koizumi, The crystal structure of BaNiO3, 1976. https://doi.org/10.1107/S056774087600798X.

[40] D. Gutiérrez-Martín, M. Parras, A. Torres-Pardo, M. Hernando, E. Matesanz, J.M. González-Calbet, D. Portehault, A. Varela, BaNiO 3 electrocatalysts for oxygen evolution reaction: the role of synthetic methods, 2024. https://doi.org/10.26434/chemrxiv-2024-n8bj6.

[41] R. Gottschall, R. Scho, M. Muhler, N. Jansen, D. Walcher, P. Gu, Electronic state of nickel in barium nickel oxide, BaNiO 3 (1998). https://pubs.acs.org/sharinggguidelines.

[42] A.M. Venezia, A. Parmaliana, A. Mezzapica, G. Deganello, Pumice-supported nickel catalysts structural and reactivity study in the hydrogenation of CO, 1997.

[43] R.B. Shalvoyand, P.J. Reucroft, B.H. Davis. Characterization of coprecipitated Nickel on Silica methanation catalysts by X-Ray photoelectron spectroscopy, 1979.

[44] H. Cheraparambil, M. Vega-Paredes, Y. Wang, H. Tüysüz, C. Scheu, C. Weidenthaler, Deciphering the role of Fe impurities in the electrolyte boosting the OER activity of LaNiO3, J. Mater. Chem. A Mater. (2024), https://doi.org/10.1039/d3ta06733e.

[45] L. Twight, A. Tonsberg, S. Samira, K. Velinkar, K. Dumpert, Y. Ou, L. Wang, E. Nikolla, S.W. Boettcher, Trace Fe activates perovskite nickelate OER catalysts in alkaline media via redox-active surface Ni species formed during electrocatalysis, J. Catal. (2024) 115443, https://doi.org/10.1016/j.jcat.2024.115443.

[46] Y. Ou, L.P. Twight, B. Samanta, L. Liu, S. Biswas, J.L. Fehrs, N.A. Sagui, J. Villalobos, J. Morales-Santelices, D. Antipin, M. Risch, M.C. Toroker, S. W. Boettcher, Cooperative Fe sites on transition metal (oxy)hydroxides drive high oxygen evolution activity in base, Nat. Commun. 14 (2023), https://doi.org/10.1038/s41467-023-43305-z.

[47] J. Deng, M.R. Nellist, M.B. Stevens, C. Dette, Y. Wang, S.W. Boettcher, Morphology dynamics of single-layered Ni(OH)2/NiOOH nanosheets and subsequent Fe incorporation studied by in situ electrochemical atomic force microscopy, Nano Lett. 17 (2017) 6922–6926, https://doi.org/10.1021/acs.nanolett.7b03313.

[48] M.L. Weber, G. Lole, A. Kormanyos, A. Schwiers, L. Heymann, F.D. Speck, T. Meyer, R. Dittmann, S. Cherevko, C. Jooss, C. Baeumer, F. Gunkel, Atomistic insights into activation and degradation of La0.6Sr0.4CoO3-δElectrocatalysts under Oxygen Evolution Conditions, J. Am. Chem. Soc. 144 (2022) 17966–17979, https://doi.org/10.1021/jacs.2c07226.

[49] K.J. May, C.E. Carlton, K.A. Stoerzinger, M. Risch, J. Suntivich, Y.L. Lee, A. Grimaud, Y. Shao-Horn, Influence of oxygen evolution during water oxidation on the surface of perovskite oxide catalysts, J. Phys. Chem. Lett. 3 (2012) 3264–3270, https://doi.org/10.1021/jz301414z.

[50] T. Quast, S. Varhade, S. Saddeler, Y.T. Chen, C. Andronescu, S. Schulz, W. Schuhmann, Single particle nanoelectrochemistry reveals the catalytic oxygen evolution reaction activity of Co3O4 nanocubes, Angewandte Chemie - Int. Ed. 60 (2021) 23444–23450, https://doi.org/10.1002/anie.202109201.